Journal of Heat and Mass Transfer Research

Journal homepage: https://jhmtr.semnan.ac.ir

Semnan University

ISSN: 2383-3068

Research Article

Investigation of a Flexible V-Fin for Heat Transfer Enhancement in a Backward-Facing Step

Ikram Djellid [a], Noureddine Bouhamri [a]*, Mohamed Bouhafs [a], Mohamed Bouzit [b], Ikram Boualem [a]

[a] *Institute of Industrial Maintenance and Safety, University of Oran 2 Mohamed Ben Ahmed, Laboratory of Production Engineering and Industrial Maintenance (LGPMI), B.P. 170 El M'naouer Oran 31000, Algeria*

[b] *Faculty of Mechanical Engineering, University of Science and Technology of Oran Mohamed Boudiaf, El M'naouer, Laboratory of Maritime Sciences and Engineering (LSIM), B.P.1505, 31000, Oran, Algeria*

ARTICLE INFO

Article history:

Received: 2025-08-20
Revised: 2025-11-06
Accepted: 2025-11-29

Keywords:

Nusselt number;
Elastic;
Forced convection;
Heat transfer;
Fin positions.

ABSTRACT

A numerical study was conducted to enhance heat transfer in a backward-facing step configuration via forced convection. Using the finite element method, simulations were performed for Reynolds numbers from 50 to 200. A flexible V-fin was introduced to direct the coolant (air) flow toward the heated wall. The fin's vertical position (y = 0, $H/10$, $H/5$) and elasticity, governed by the Cauchy number (Ca = 10^{-4}, 10^{-5}, 10^{-6}, 10^{-7}), were key variables. The optimal configuration (y = $H/5$, Ca = 10^{-7}, Re = 200) yielded a 30.75% increase in the average Nusselt number over the baseline without a fin. The results confirm that the fin consistently improves thermal performance, whether rigid or flexible. This study employs finite element simulations to analyze forced convection heat transfer in a backward-facing step channel. The research investigates the effect of a flexible V-fin. compared to the case without a fin. Crucially, the fin's presence improved heat transfer performance regardless of its rigidity.

1. Introduction

Investigations of heat transfer, convection, and related fluid flow phenomena have contributed to improved energy performance and solutions to heat-dissipation problems in energy storage, electronic coolers, heat exchangers, and many high-tech applications. In keeping with these advancements, researchers have recently turned their interest toward studying the interaction between fluids and structures and their effects on heat transfer in thermal systems.

Numerous studies have examined non-Newtonian fluid flow and heat transfer in cavities with deformable structures such as flexible fins and membranes [1-3]. These works have shown that fin deflection increases in dilatant fluids, that the effect of the power-law index on heat transfer is minor, that a stiff fin enhances the Nusselt number by about 2.6-7%, and that optimal heat transfer occurs at St = 0.20 with L_f=0.6. Transient and mixed convection phenomena as well as the effect of fluid–elastic wall interaction on heat transfer enhancement have been widely studied [4-7]. These works reported that wall

* **Corresponding author.**
E-mail address: *bouhamri.noureddine@univ-oran2.dz*

Cite this article as:
Djellid, I., Bouhamri, N., Bouhafs, M., Bouzit, M. and Boualem, I., 2026. Investigation of a Flexible V-Fin for Heat Transfer Enhancement in a Backward-Facing Step. *Journal of Heat and Mass Transfer Research*, 13(3), pp. 295-313.
https://doi.org/10.22075/JHMTR.2025.38745.1809

deformation and fin oscillation can markedly improve heat transfer, with average Nusselt numbers rising by up to 17% compared with rigid configurations, and by about 3-4% when the oscillation amplitude reaches 0.1. Fin flexibility and counter-rotating flow were also found to increase entropy generation and heat transfer at higher Rayleigh numbers, while excessive elasticity reduced performance at very high Richardson numbers. Finite Element, Arbitrary Lagrangian-Eulerian, and smoothed particle hydrodynamics methods have been effectively employed to model such transient thermo-fluid interactions and predict the associated flow patterns and structural responses [8-11]. Researchers have aimed to couple the synergistic interactions between fluids and structures to enhance heat transfer by adjusting the flexibility and material properties of these components [12-14]. Studies have shown that asymmetric flag arrangements can improve cooling performance through better vortex mixing, achieving maximum convective enhancement at Re = 600 with bending rigidity of $\gamma = 0.04$. In addition, experiments on flexible T-shaped beams reported that deformation increased by nearly 90% as the flow velocity rose from 0.25 to 0.35 m/s, demonstrating the strong dependence of structural response on flow conditions.

A variety of cavity configurations, including square and inclined cavities with elastic membranes, oscillating fins, and deformable baffles, have been explored to study transient natural convection [15-18]. These studies revealed that flexible and oscillating components significantly alter flow structures and heat transfer, with fin oscillation and wall deformation notably enhancing natural convection as the Rayleigh number increases. In oblique cavities, oscillating fins and flexible membranes were shown to strongly influence temperature distribution and flow behavior, while increasing the Rayleigh number or baffle length further improved heat transfer and the deformation of elastic parts. Advanced computational approaches, such as the Finite Element and Galerkin methods, combined with the Arbitrary Lagrangian-Eulerian (ALE) framework, were employed to accurately capture these thermo-fluid–structure interactions.

The impact of flexible components such as heating plates, thin fins, and baffles on convective heat transfer in cavities with different geometries has also been examined [19-21]. These studies have shown that the position and inclination of a flexible heater plate significantly influence both stress and heat transfer, with maximum stress occurring at an inclination angle of about 40°, while vertical placement minimizes deformation. In addition, the inclusion of nanoparticles was found to enhance the average Nusselt number across all Reynolds numbers, with Cu and Ag nanoparticles providing the greatest improvement outside the recirculation zones. These studies highlight the importance of considering structural flexibility and vibration parameters for the accurate prediction of convective heat transfer behavior. Khanafer and Vafai [22] and Ghalambaz et al. [23] conducted numerical analyses to investigate the effectiveness of elastic walls and baffles in optimizing heat transfer in cavities filled with porous media. These studies offer insight into how obstacle bodies improve heat transfer compared to flexible wall models, as well as the effects of barrier stiffness and Rayleigh number on fluid flow patterns and convective heat transfer rates.

Prior studies [24, 25] investigated free convective heat transfer in heated flexible thin-walled cavities and MHD mixed convection in nanofluid-filled cavities with flexible sidewalls. These studies have shown trends such as the effect of the power-law exponent on fluid circulation and heat transfer rates, as well as improved heat transfer with increasing nanoparticle size fraction. Studies by [26-28] investigated the effects of parameters such as the Hartmann number, tilt angle, and nanoparticle concentration on heat transfer characteristics in ferrofluid and rotating cylinder scenarios. These studies highlight the significant effects of the external magnetic field, cylinder rotation, and nanoparticle size fraction on convective heat transfer, paving the way for customized thermal management strategies. Studies by [29-32] also addressed the effects of nanofluid properties, channel geometry, and flow regimes on heat transfer rates. In particular, these studies revealed the relationship between nanoparticle size, Reynolds number, and Nusselt number enhancement and provided valuable insights into the design of efficient heat exchangers and thermal systems.

Studies by [33-35] have also examined the effects of geometric modifications such as wavy walls and sudden expansions on flow structure and heat transfer. It was reported that applying a magnetic field reduces the recirculation zone while enhancing heat transfer for fluids with high Prandtl numbers. Introducing corrugated walls downstream of a backward-facing step increased the Nusselt number by up to 62% at Re = 5000, with optimal improvement achieved at a corrugation height of 4 mm. Furthermore, variations in the expansion ratio were found to strongly influence the reattachment length and flow instability, directly affecting the distribution of the Nusselt number and skin friction. Alhasan et al. [36] conducted additional numerical

modifications to the geometry, such as introducing a moving belt with different velocities. These studies highlight the effectiveness of innovative geometries in improving convective heat transfer while minimizing pressure losses, offering promising opportunities for practical applications.

Furthermore, Atashafrooz [37] and Danane et al. [38] examined the effects of the interaction between radiative heat transfer, Brownian motion, and external magnetic fields on the heat transfer properties of nanofluids. These studies highlighted the complex coupling between different transport phenomena and revealed the mechanisms governing heat transfer enhancement in complex fluid systems. Studies [39, 40] focused on entropy generation and heat transfer in pulsating flow regimes and elucidated the effects of flow pulsations and magnetic fields on flow behavior and thermal properties. These studies provide valuable insights into optimizing heat transfer processes in dynamic flow environments.

Several passive methods to enhance heat transfer in backward-facing step (BFS) geometries have been proposed in recent research, including porous media and surface modifications. Ideal porous baffles, such as upper-wall, quarter-circular, and corrugated designs, were found to significantly enhance local Nusselt numbers [41], and a semi-porous baffle located downstream of the step improved average and peak heat transfer by up to 90% at low Darcy numbers [42]. Gradient and multilayer porous foams were also optimized to achieve maximum heat transfer using low pumping power, demonstrating a threefold performance improvement when used with nanofluids [43, 44]. Furthermore, grooved surfaces effectively induced fluid mixing and convection, and circular and semicircular grooves achieved as much as a 9.6% increase in the Nusselt number for Al_2O_3 water nanofluids [45, 46].

Most BFS studies employ either rigid or porous inserts; the influence of flexible fins on the airflow and heat transfer is not well understood. This study examines the position and stiffness effects of a deforming V-shaped fin on recirculation and thermal performance in an air-filled BFS and presents a new passive approach for enhancing heat transfer. In the present work, the problem of forced air convection in a backward-facing step disturbed by a flexible fin mounted at three different locations was numerically investigated in order to explain the effects of fin placement and elasticity on flow structures and heat-transfer behavior. The results will contribute to the development of high-performance thermal systems utilizing BFS geometries and flexible flow-control devices.

2. Problem Description

2.1. Geometric Configuration of the Problem

The flow of an incompressible fluid (air) under forced convection in a backward-facing step (BFS) with a V-shaped fin is studied numerically in two dimensions in this paper.

Figure 1 displays the boundary conditions and the physical setup. The height of the backward step is H, the height of the channel is $2H$, the bottom wall is maintained at a hot temperature (T_h), and T_c is the input temperature where the flow is cold. The rest of the walls are adiabatic and are modeled with no-slip conditions. At the inlet, the velocity is $u=U_0$ and $v=0$. At the outlet, both the gradient of velocity in the x direction and the gradient of temperature are set to zero.

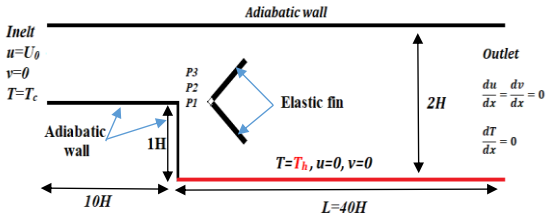

Fig. 1. Geometry of the problem with boundary conditions

3. Governing Equations

3.1. Governing Dimensionl Equations

The governing equations for fluid flow, heat transfer, and structural response of the system are presented below. The first of these is the continuity equation, Eq. (1), which ensures mass conservation and is given by [36]:

- **Continuity equation**

$$\frac{\partial u}{\partial x}+\frac{\partial v}{\partial y}=0 \tag{1}$$

- **Momentum equations (Navier-Stokes)**

$$\rho\left(\frac{\partial u}{\partial t}+u\frac{\partial u}{\partial x}+v\frac{\partial u}{\partial y}\right)=-\frac{\partial p}{\partial x}+\mu\left(\frac{\partial^2 u}{\partial x^2}+\frac{\partial^2 u}{\partial y^2}\right) \tag{2}$$

$$\rho\left(\frac{\partial v}{\partial t}+u\frac{\partial v}{\partial x}+v\frac{\partial v}{\partial y}\right)=-\frac{\partial p}{\partial y}+\mu\left(\frac{\partial^2 v}{\partial x^2}+\frac{\partial^2 v}{\partial y^2}\right) \tag{3}$$

- **Energy equation**

$$\frac{\partial T}{\partial t}+u\frac{\partial T}{\partial x}+v\frac{\partial T}{\partial y}=\alpha\left(\frac{\partial^2 T}{\partial x^2}+\frac{\partial^2 T}{\partial y^2}\right) \tag{4}$$

The deformation of the elastic fin under the influence of fluid forces is described by the elastic dynamic equation [2].

$$\rho_S \frac{\partial^2 d_S}{\partial t^2} - \nabla^2 \sigma = 0 \tag{5}$$

in this formulation, ρ_S stands for the density of the solid material, d_S denotes its displacement vector, and σ represents the Cauchy stress tensor. The latter is described through a nonlinear elasticity model, expressed as:

$$\sigma = J^{-1} FSF^T \tag{6}$$

$F = I + \nabla d_s$ correspond to the deformation gradient, $J = \det(F)$ is the Jacobian determinant, and S refers to the second Piola-Kirchhoff stress tensor, which can be written as:

$$S = C:(\varepsilon), \varepsilon = \frac{1}{2}(\nabla d_S + \nabla^T d_S + \nabla^T d_S \nabla d_S) \tag{7}$$

$C = C(E,\upsilon)$ is the fourth-order elasticity tensor, defined as a function of the Young's modulus E and Poisson's ratio υ, while ε designates the Green-Lagrange strain tensor. The dimensional boundary conditions are presented in Table 1.

Table 1. Dimensional boundary conditions

At inlet	$u = u_0,\ v = 0,\ T = T_c$
At outlet	$\frac{\partial u}{\partial n} = \frac{\partial v}{\partial n} = \frac{\partial T}{\partial n} = 0$
In bottom wall	$u = 0, v = 0, T = T_h$
Remaining walls are adiabatic, with a no-slip velocity condition	$u = v = 0, \frac{\partial T}{\partial n} = 0.$
Adiabatic fin	$\frac{\partial T}{\partial n} = 0$

3.2. Governing Dimensionless Equations

In order to transform the governing equations into their non-dimensional form, this study employs the following parameters [2]:

$$(X, Y, D_S) = \frac{(x, y, d_S)}{H},\ \mathrm{P} = \frac{p}{\rho U_0^{\,2}},\ (U, V) = \frac{(u, v)}{U_0},$$

$$\theta = \frac{T - Tc}{Th - Tc},\ \tau = \frac{(tU_0)}{H},\ \rho_r = \frac{\rho}{\rho_S},\ \alpha_r = \frac{\alpha_s}{\alpha_f}$$

Prandtl number $\mathrm{Pr} = \frac{\mu Cp}{k}$

Cauchy number $Ca = \frac{\rho U_0^{\,2}}{E}$

Reynolds number $\mathrm{Re} = \frac{\rho U_0 H}{\mu}$

- **Continuity equation**

$$\frac{\partial U}{\partial X} + \frac{\partial V}{\partial Y} = 0 \tag{8}$$

Navier-Stokes equations, Eqs. (9) and (10), describe the conservation of momentum in the *X* and *Y* directions. These equations are based on contributions of convective terms to flow, pressure gradients, and viscous diffusion terms which are governed by the Reynolds number (*Re*) [36]:

- **Navier-Stokes equations**

$$\frac{\partial U}{\partial \tau} + U\frac{\partial U}{\partial X} + V\frac{\partial U}{\partial Y} = -\frac{\partial P}{\partial X} + \frac{1}{\mathrm{Re}}\left(\frac{\partial^2 U}{\partial X^2} + \frac{\partial^2 U}{\partial Y^2}\right) \tag{9}$$

$$\frac{\partial V}{\partial \tau} + U\frac{\partial V}{\partial X} + V\frac{\partial V}{\partial Y} = -\frac{\partial P}{\partial X} + \frac{1}{\mathrm{Re}}\left(\frac{\partial^2 V}{\partial X^2} + \frac{\partial^2 V}{\partial Y^2}\right) \tag{10}$$

The temperature field of the fluid is governed by the energy equation Eq. (11); including the convective heat transfer and diffusion effects with the Prandtl number (*Pr*) [36]:

- **Energy equation**

$$\frac{\partial \theta}{\partial \tau} + U\frac{\partial \theta}{\partial X} + V\frac{\partial \theta}{\partial Y} = \frac{1}{\mathrm{Re}\,\mathrm{Pr}}\left(\frac{\partial^2 \theta}{\partial X^2} + \frac{\partial^2 \theta}{\partial Y^2}\right) \tag{11}$$

Elastodynamic domain [2]:

$$\frac{Ca}{\rho_r}\frac{\partial^2 D_s}{\partial \tau^2} - \nabla \sigma_s = 0 \tag{12}$$

The average and local Nusselt numbers along the heated bottom wall, which is obtained from the statement [47], determine the heat transfer efficiency:

$$Nu_X(X) = -\left(\frac{\partial \theta}{\partial Y}\right) = \frac{hH}{k} \tag{13}$$

The average Nusselt number (Nu_{avg}) is defined as follows [47]:

$$Nu_{avg} = \frac{1}{L}\int_0^L Nu_X(X)\,dX \tag{14}$$

where *L* is the length of the bottom hot wall. The dimensionless boundary conditions are summarized in Table 2.

Table 2. Dimensionless boundary conditions

At inlet	U = U_0, V = 0, θ = 0.
At outlet	$\frac{\partial U}{\partial n} = \frac{\partial V}{\partial n} = \frac{\partial \theta}{\partial n} = 0$
In the bottom wall	$U = V = 0, \theta = 1$
The remaining walls are adiabatic, with a no-slip velocity condition applied.	$U = V = 0, \frac{\partial \theta}{\partial n} = 0$
Fin adiabatic	$\frac{\partial \theta}{\partial n} = 0$

The governing equations are solved numerically using the Finite Element Method (FEM) in a transient framework. The laminar flow and heat transfer equations are coupled with the solid mechanics equations of the flexible fin through a Fluid-Structure Interaction (FSI) formulation based on the Arbitrary Lagrangian-Eulerian (ALE) approach. A time-dependent solver was employed to capture the deformation of the elastic fin under the action of fluid forces until a steady configuration was achieved.

The nonlinear system was handled with a fully coupled iterative scheme using a relative tolerance of 10^{-6}. The final results were extracted once both the fin deformation and the global flow and thermal fields reached steady behavior. The accuracy of this numerical solution was further assessed through a mesh independence test, as discussed in the following section.

4. Mesh Testing

A structured triangular mesh was generated, with local refinement near the walls and around the fin to better resolve the strong gradients in velocity and temperature (Fig. 2). To verify the reliability of the numerical results, a mesh independence test was conducted using six different grid sizes at Re = 100 and Pr = 0.71.

As mentioned in Table 3, the average Nusselt number and dimensionless pressure drop (ΔP) showed negligible variation between the last two grids; therefore, the penultimate mesh, containing 226,301 elements, was adopted for all subsequent simulations to achieve a balance between accuracy and computational cost. The convergence of the numerical solution was further ensured by monitoring the residuals of the governing equations and by confirming the consistency of the overall heat flux across the computational boundaries.

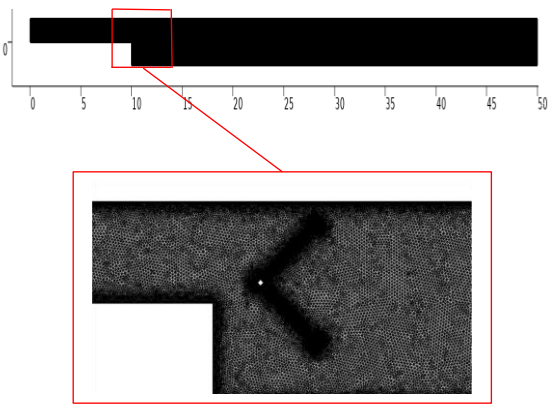

Fig. 2. The mesh generation of the computational domain

Table 3. The convergence test of grid

Number of element	Nu_{avg}	ΔP
25147	0.9796	2.7705
46859	0.9946	2.7554
78340	0.9982	2.7398
166157	0.9995	2.7010
226301	**1.0001**	**2.6926**
292554	1.0009	2.6928

5. Results and Discussion

5.1. Validation of Results

For an adequate analysis of the results sought, it is preferable to start with a validation of our model against the studies treated by [47] and [36]. As shown in Fig. 3, the variation of the Nusselt number along the x-direction in our simulation exhibits the same general trend as that reported in the works of Kumar and Dhiman [47] and Alhasan et al. [36], for the control parameters Re = 200 and Pr = 0.71. A sharp increase is observed, reaching a maximum value of 2.3 at x/H = 8.2, followed by a gradual decrease to about Nu = 0.85. The agreement between the results is evident, with both curves displaying comparable behavior, with the exception of the spade, where there is a difference in value of 2.3 for our case and 2.44 for Kumar's case and 2.42 for Alhasan et al case, resulting in an error of less than 5.73 % and 4.96%, respectively. A second validation test was performed using the reattachment length for the reference backward-facing step case at Re=100 and an expansion ratio of 2 (ER=2). The obtained reattachment length was compared with the results of previous works [47] and [36]. As shown in Table 4, the present values are in close agreement with these studies, with deviations of 0.08% and 2.65%, respectively. These comparisons confirm that our model is well-validated against the existing data, providing confidence for the subsequent investigation.

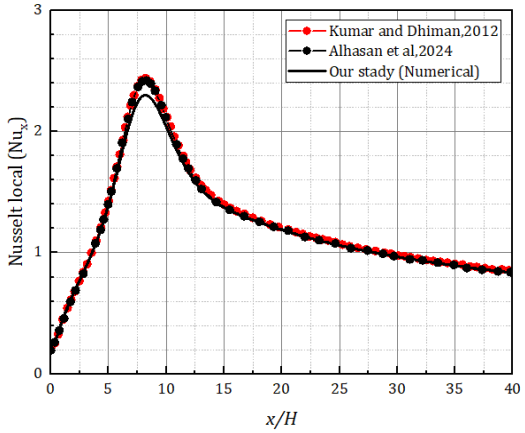

Fig. 3. Comparison of local Nusselt number with [47] and [36]

Table 4. Validation of the eattachment length value X_r at Re=100 and ER=2

Study	X_r/H	Error %
Present study	4.9858	0
Kumar and Dhiman [41]	4.9898	0.08
Alhasen et al. [36]	5.118	2.65

A non-stationary study was conducted to investigate the effects of fin elasticity and position in a BFS on heat transfer optimization. The Cauchy number values (10^{-4}, 10^{-5}, 10^{-6}, and 10^{-7}) were considered, in addition to the Reynolds number (50, 100, 150, and 200) and three changes in position relative to the y-axis (position 1, y=0, position 2, $y=H/10$, and position 3, $y=H/5$) at x=10.5H. The results, obtained via transient numerical calculations, are presented in the form of streamlines and isotherms in Figs. 4-10, the average Nusselt number in Figs. 11-13, the local Nusselt number in Figs. 14-16, and finally the maximum Nusselt number in Fig. 17.

5.2. Presentation of the Unsteady States

This type of simulation is initially transient and prone to oscillation. However, over time, both the fluid flow and the fin deformation reach a stable, periodic state.

Figure 4 shows the streamlines at various dimensionless times for a constant Reynolds number (Re=150), fin position 3 ($y=H/5$), and Pr=0.71 varying the Cauchy number (Ca=10^{-4}, 10^{-5}, 10^{-6}, 10^{-7}). The figures show the deformation of the fin, which continues to deform in the direction of flow until it reaches stability, due to fluid pressure and viscous drag. The deformation continues until it reaches a maximum value and, after a short time, it returns to a permanently stabilized position.

The effect of elasticity on vortex length is clearly apparent. When the fin is highly elastic ($Ca = 10^{-4}$), the inward deformation of the two branches of the fin causes the formation of a larger vortex. Decreasing the elasticity of the fin reduces the length of the vortex. Beyond $Ca = 10^{-5}$, no deformation of the fin is observed, and elasticity has no further effect on the length of the vortices.

5.3. Streamlines and Isotherms

In the field of Fluid-Structure Interaction, the fluid parameter with the greatest influence on this physical phenomenon is inertia, which is represented by the Reynolds number. In numerical studies, researchers frequently use the term 'inertia' to describe the Reynolds number's effect on the hydrodynamic structure of a flow, the thermal behavior of the geometry, and the elastic deformation of the structure. The Reynolds number illustrates the relationship between the inertia and viscosity forces. Furthermore, as the flowing fluid is Newtonian and its viscosity remains constant, the effect of inertia becomes the predominant parameter. Consequently, a change in the Reynolds number corresponds to a change in the inlet velocity at the backward-facing step.

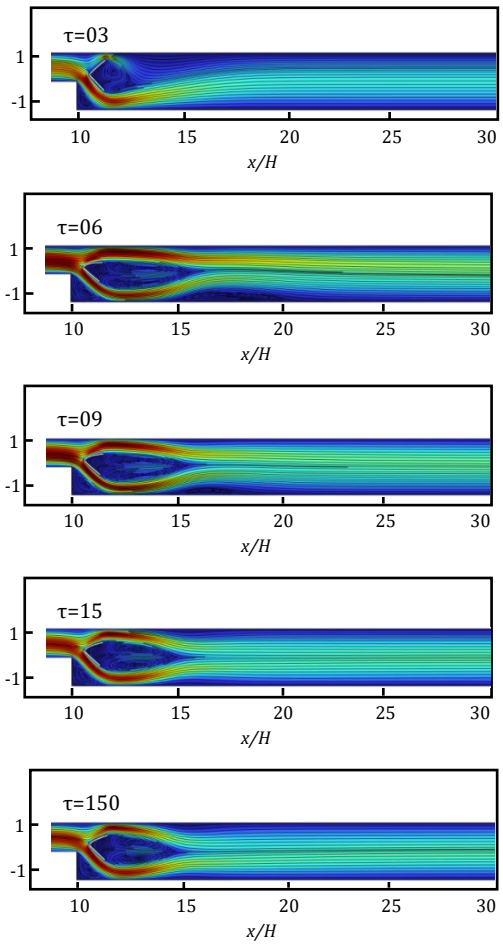

(a) Ca=10^{-4}

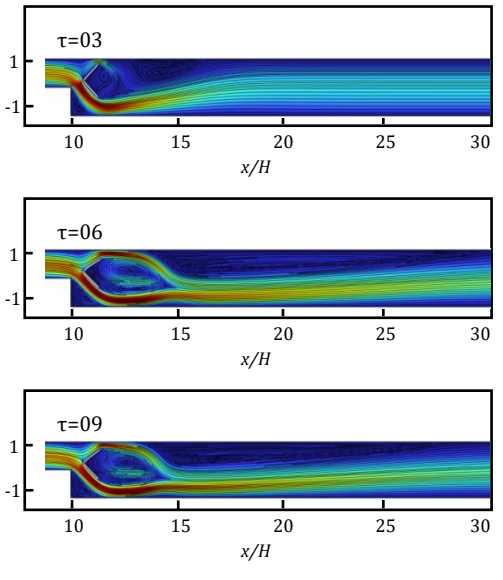

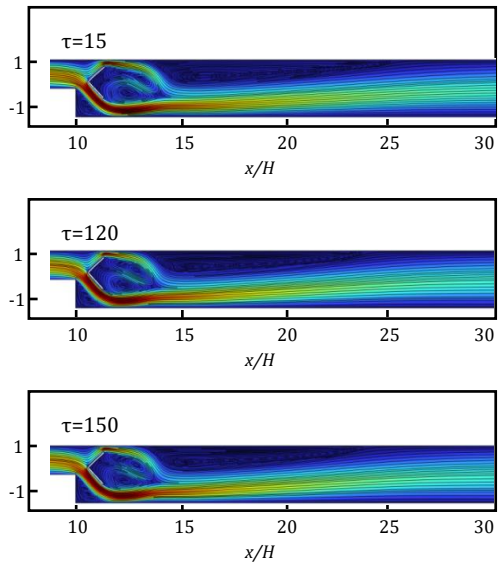

(b) Ca=10^{-5}

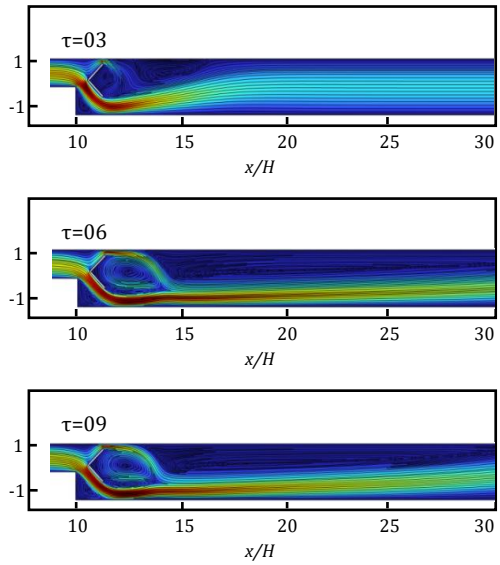

(c) Ca=10^{-6}

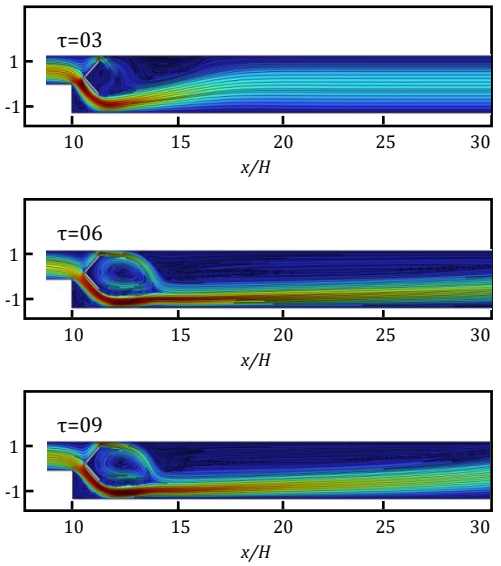

(d) Ca=10^{-7}

Fig. 4. Temporal evolution of streamlines at various Cauchy numbers for Re = 150 at position 3

Figures 5-7 illustrate the streamline patterns for various Reynolds and Cauchy numbers at different flexible fin positions. As the Reynolds number increases, the main vortex behind the fin becomes larger and stronger due to enhanced inertial effects. In contrast, higher fin flexibility (larger Cauchy number) suppresses vortex intensity, leading to smaller recirculation zones.

When the fin becomes rigid (lower Cauchy number), additional secondary vortices appear near the bottom wall at position 1 and near the top wall at positions 2 and 3, with their size increasing as stiffness increases. These results emphasize the strong influence of fin flexibility and placement on the flow structure and recirculation behavior.

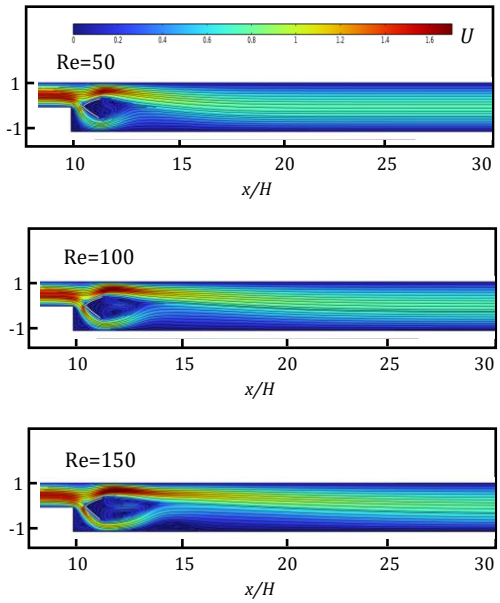

(a) Position 1 (y=0)

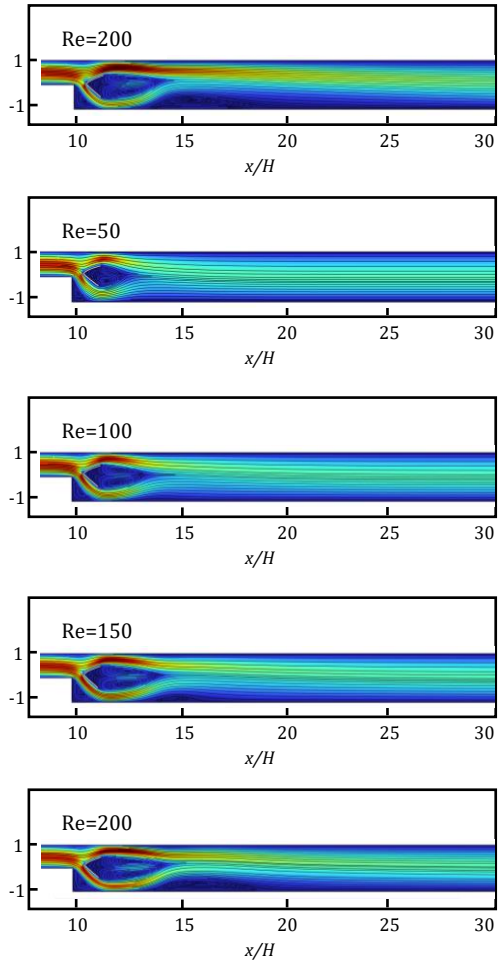

(b) Position 2 (y=H/10)

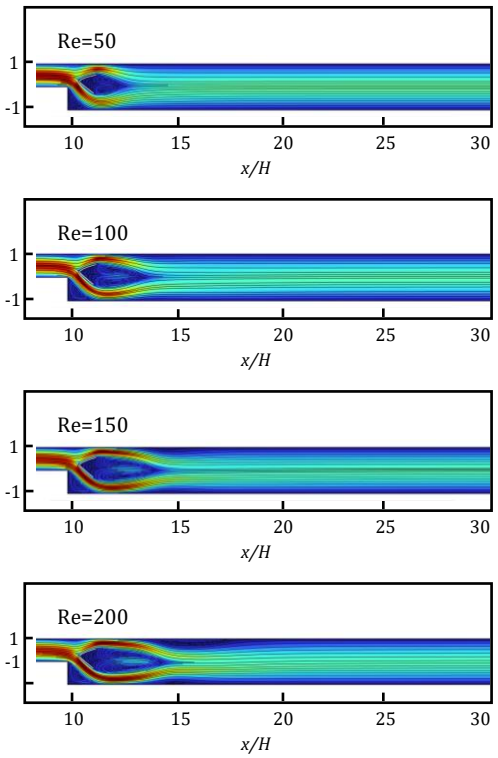

(c) Position 3 (y=H/5)

Fig. 1. Streamlines for different positions and Reynolds numbers at $Ca = 10^{-4}$

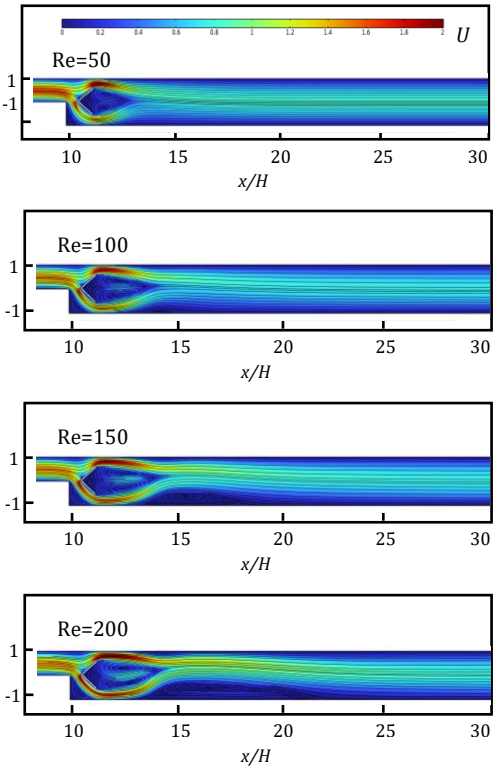

(a) Position 1 (y=0)

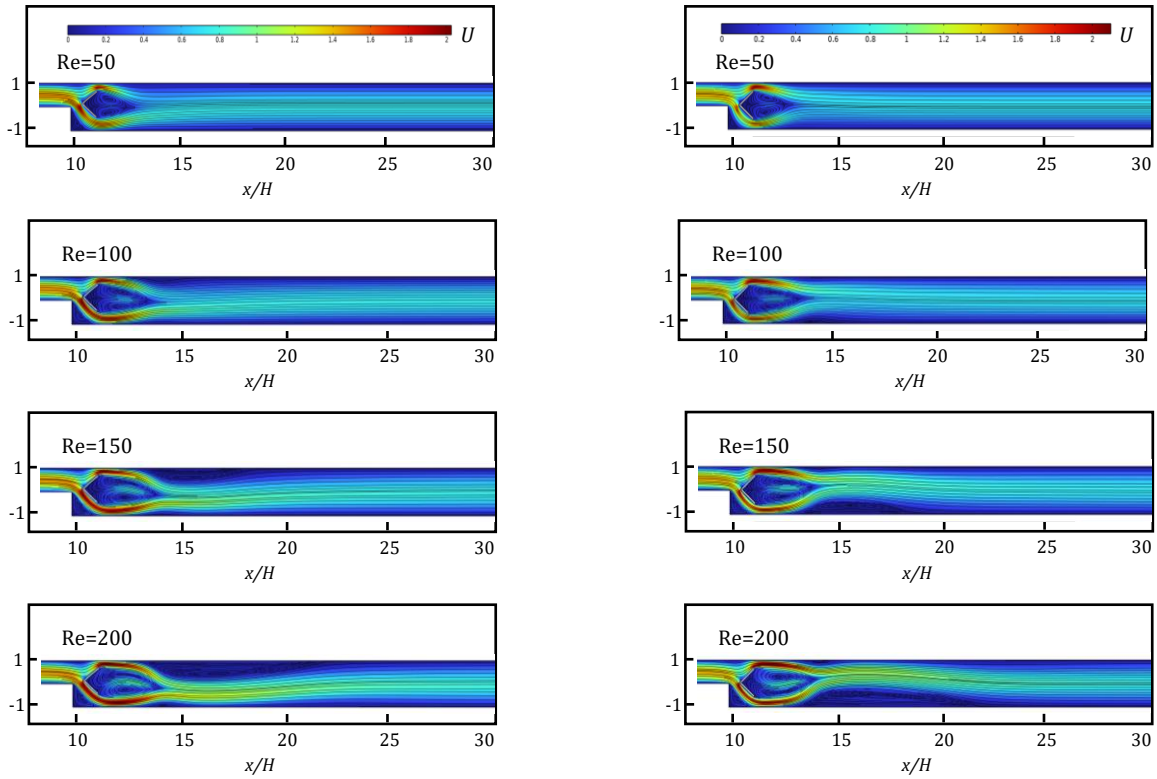

(b) Position 2 (y=H/10) **(a) Position 1 (y=0)**

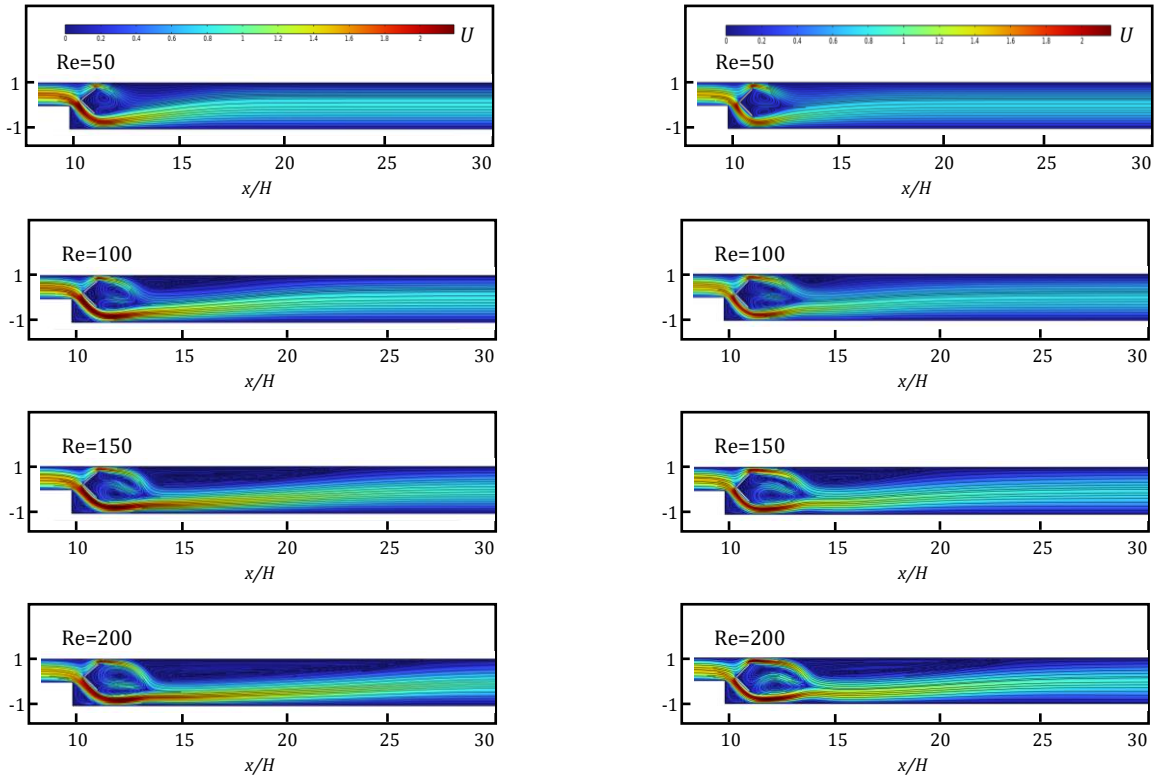

(c) Position 3 (y=H/5) **(b) Position 2 (y=H/10)**

Fig. 2. Streamlines for different positions and Reynolds numbers at $Ca = 10^{-5}$

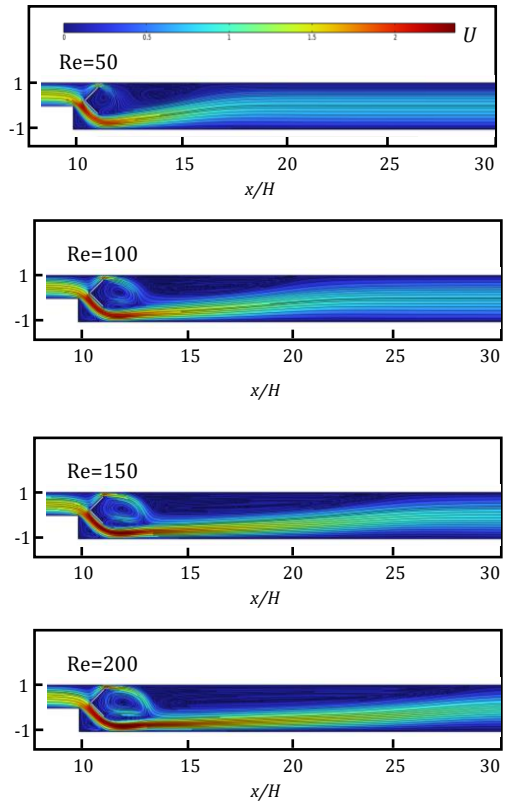

(c) Position 3 (y=H/5)

Fig. 3. Streamlines for different positions and Reynolds numbers at Ca =10^{-7}

Figures 8-10 present the temperature contours observed inside the backward-facing step for different Reynolds and Cauchy numbers and for several positions of the flexible fin. When comparing these cases, it is evident that the Cauchy number has only a limited effect on the overall temperature distribution, since the general pattern of the isotherms remains almost unchanged. This behavior indicates that, in the examined range, the fin's elasticity does not greatly alter the thermal field. However, the location of the flexible fin and the flow intensity, expressed by the Reynolds number, have a significantly more visible influence. As the Reynolds number increases from 50 to 200, the hot region close to the heated wall gradually decreases in size, suggesting a stronger convective motion and better penetration of the cold fluid into the lower zone of the step. This tendency becomes more pronounced when the fin is positioned at y=H/5, where the boundary layer near the hot wall becomes noticeably thinner. At higher flow intensities, especially for Re=200 and Ca=10^{-7}, a strong recirculating vortex develops above this region. This vortex improves the mixing of the fluid and enhances the replacement of warmer fluid with colder fluid from the upstream section. Overall, the interaction between the fin's motion and the flow structure creates a complex dynamic that governs the temperature field and significantly affects the local heat transfer characteristics.

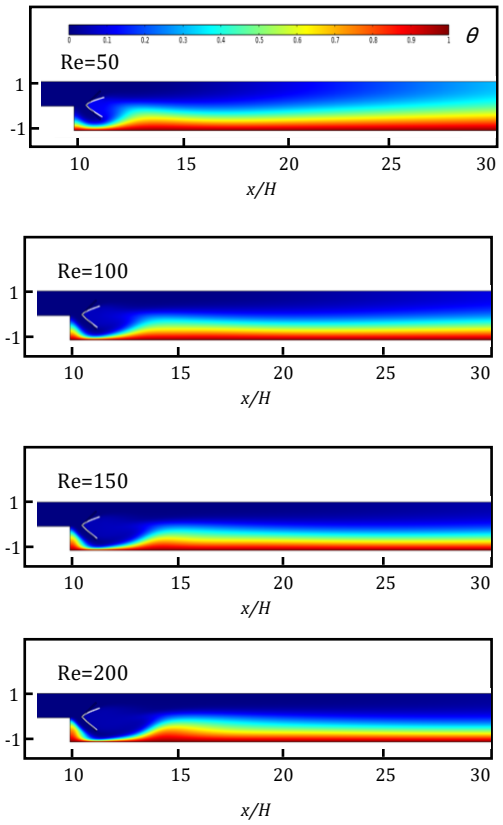

(a) Position 1 (y=0)

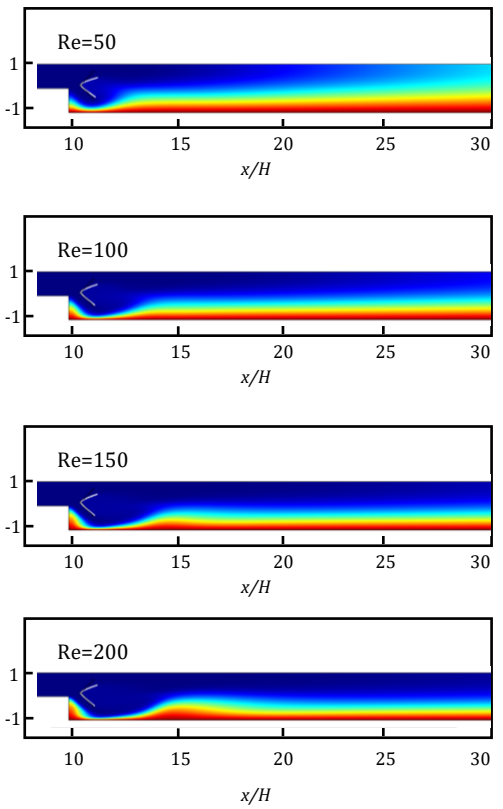

(b) Position 2 (y=H/10)

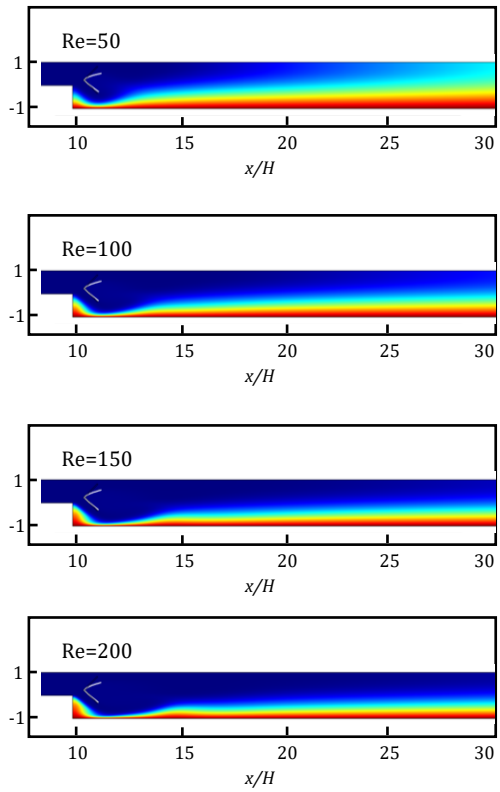

(c) Position 3 (y=H/5)

Fig. 4. Isotherms for different positions and Reynolds numbers at $Ca = 10^{-4}$

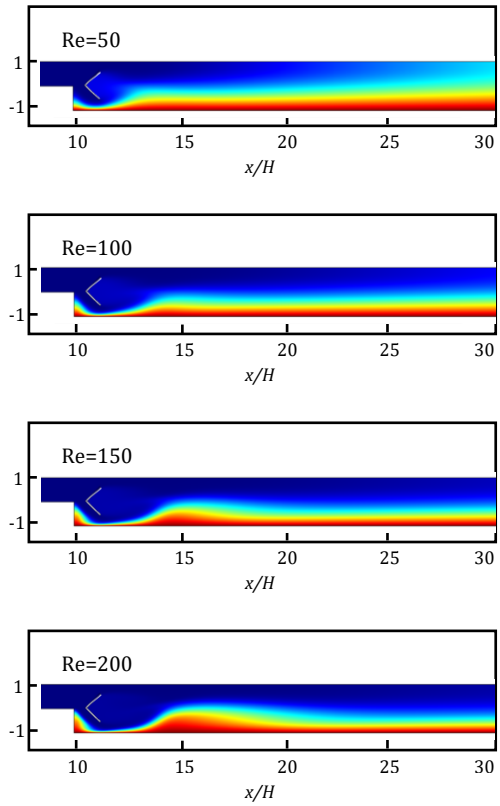

(a) Position 1 (y=0)

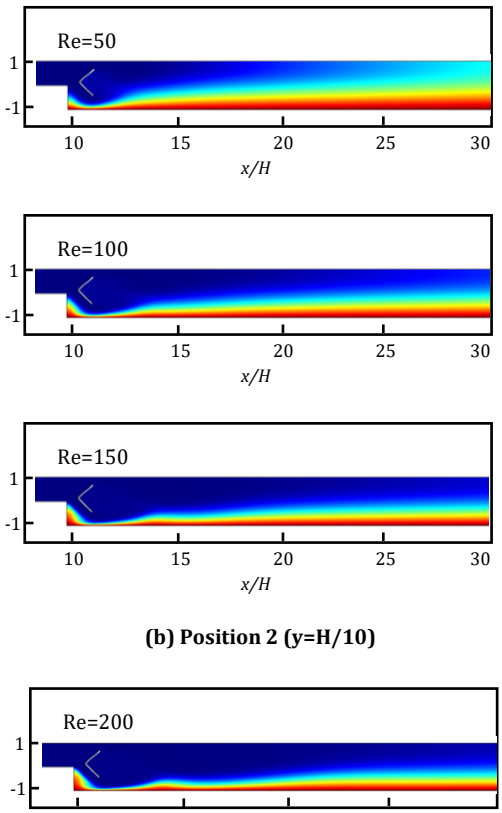

(b) Position 2 (y=H/10)

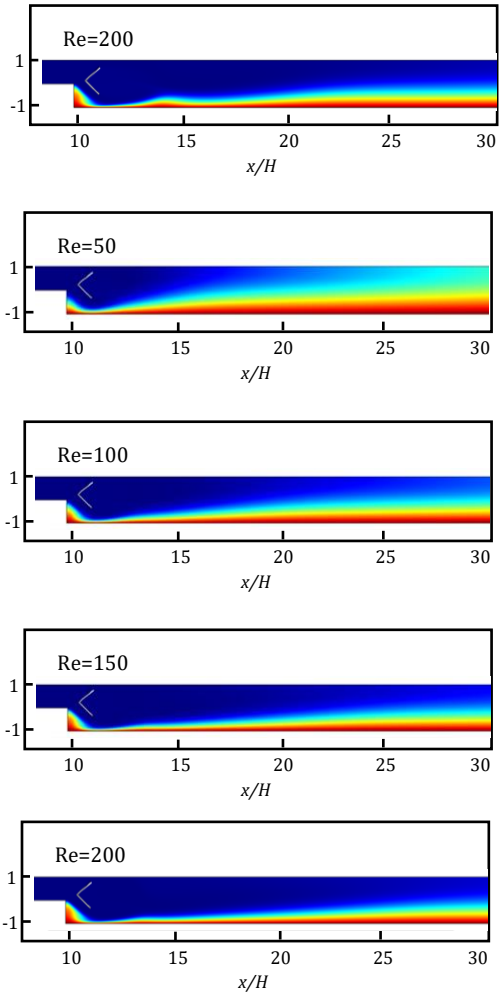

(c) Position 3 (y=H/5)

Fig. 5. Isotherms for different positions and Reynolds numbers at $Ca=10^{-5}$

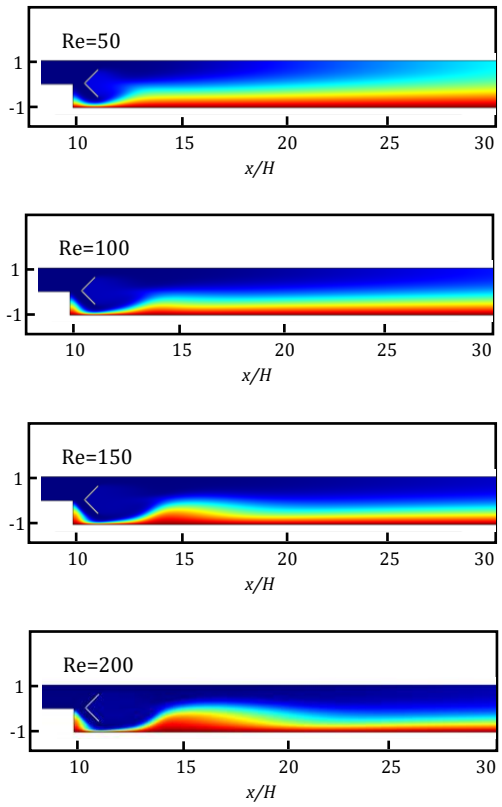

(a) Position 1 (y=0)

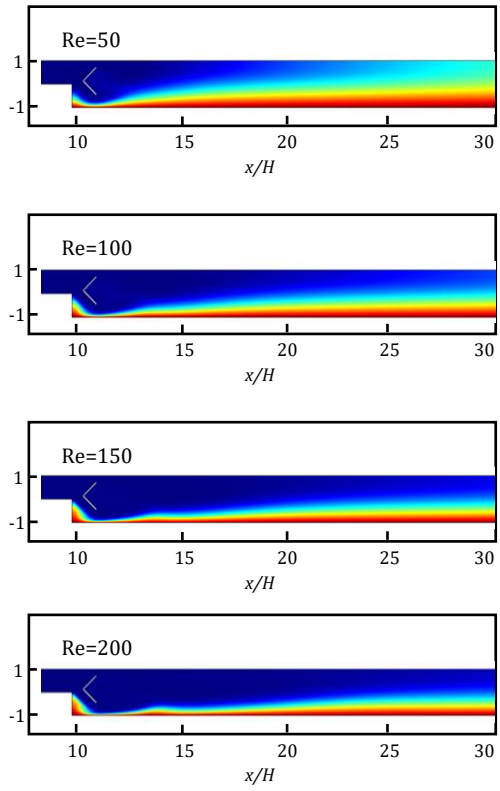

(b) Position 2 (y=H/10)

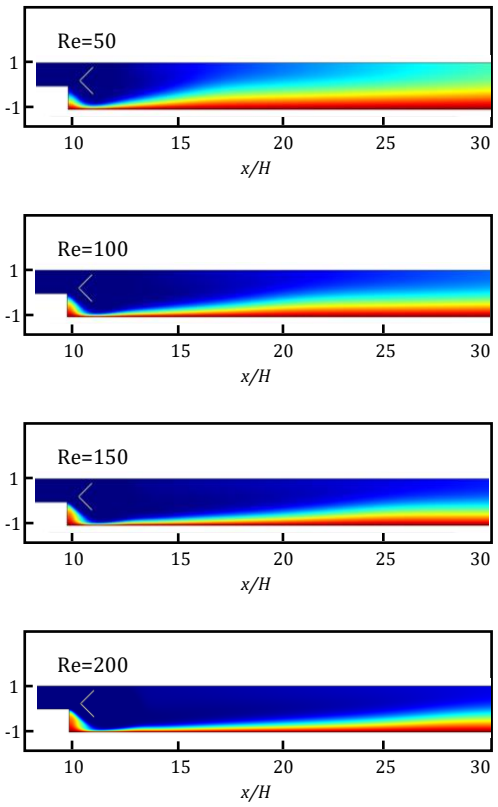

(c) Position 3 (y=H/5)

Fig. 6. Isotherms for different positions and Reynolds numbers at Ca=10^{-7}

5.4. Average Nusselt Number

The variation of the average Nusselt number with the Reynolds number is presented in Figures 11a-11c for three fin positions along the y-axis. The Prandtl number is fixed at 0.71, while the Cauchy number varies from 10^{-4} to 10^{-7}; the case without a fin is also included for comparison. All curves exhibit a similar parabolic trend, demonstrating a gradual increase in the Nusselt number with Reynolds number. At low Reynolds numbers (Re=50), the results remain almost identical for all configurations, indicating a negligible influence of fin flexibility on heat transfer.

As the Reynolds number increases, distinct variations appear among the cases, mainly due to the combined effects of flow inertia and fin motion. The interaction between the main flow and the fin enhances mixing and reduces the thermal boundary layer thickness, resulting in improved convective heat transfer near the heated wall.

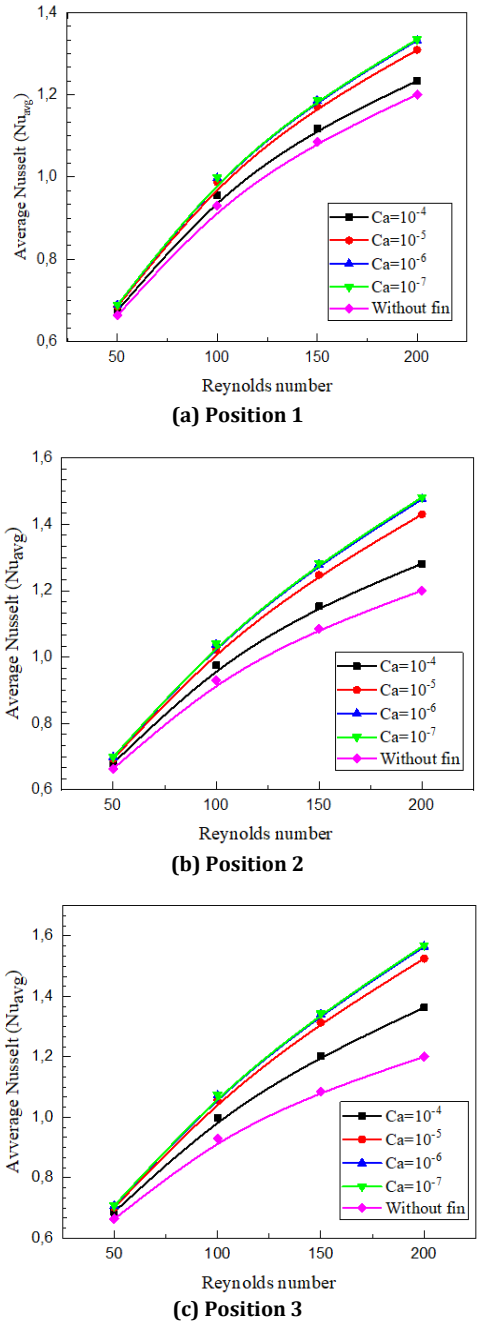

Fig. 7. Variation of the average Nusselt number with Reynolds number for various Cauchy numbers

Figures 12(a) and 12(b) compare the variation of the average Nusselt number with the Reynolds number for two Cauchy numbers and three fin positions. The position of the fin clearly matters. We observe that for low Reynolds numbers (Re=50), the fin position has a negligible effect on the average Nusselt number; however, increasing the Reynolds number reveals the distinct influence of the fin position. For all Cauchy numbers, when Re is greater than 50, position 3 yields a higher average Nusselt number than position 2, and even higher than position 1.

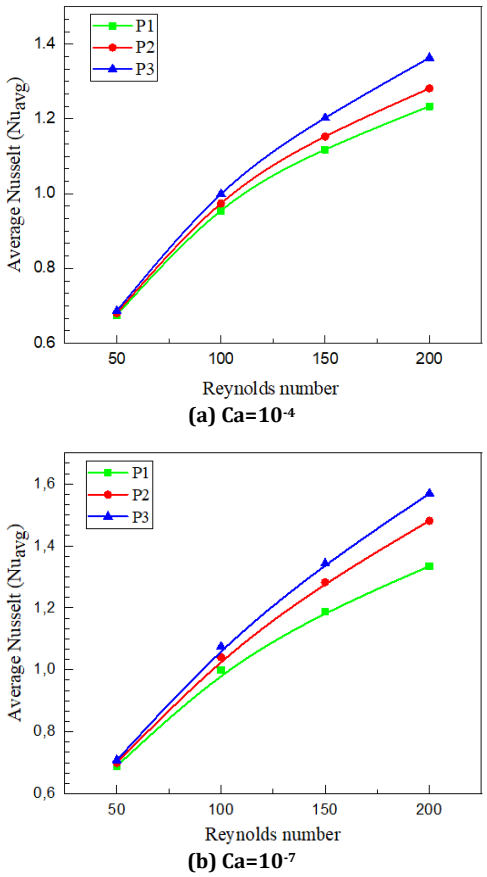

Fig. 8. Variation of the average Nusselt number with Reynolds number for (a) Ca=10^{-4}; (b) Ca=10^{-7}

Figures 13(a) and 13(b) present the variation of the average Nusselt number with the Cauchy number for two flow regimes, Re=150 and Re=200, considering the three fin positions. It can be observed that for all cases, the Nusselt number gradually decreases as the Cauchy number increases, showing a slightly curved trend. Each position keeps its own behavior, but the same general tendency is visible. For Re=150, the highest heat transfer rates occur when the fin is least flexible (Ca=10^{-7}), where the Nusselt number ranges from around 1.18 at P1 to about 1.34 at position 3. When the flow speed increases to Re=200, these values rise to approximately 1.33 and 1.57, respectively, for the same positions, representing an increase between 13.56% and 18.04%. This suggests that a rigid fin improves the heat exchange by maintaining a stronger interaction between the fluid and the heated wall.

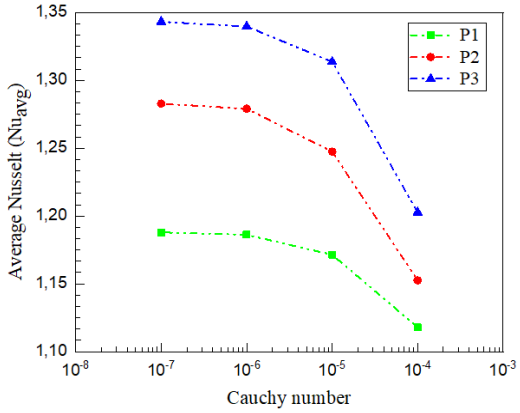

(a) *Re*=150

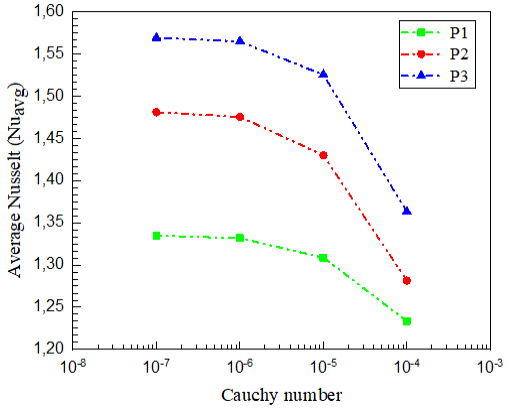

(b) *Re*=200

Fig. 9. Variation of the average Nusselt number with Cauchy number for (a) *Re*=150; (b) *Re*=200

5.5. Local Nusselt Number

After discussing the mean Nusselt number, our attention was directed toward the behavior of the local Nusselt number along the x-direction. These results are examined for various Reynolds numbers (50, 100, 150, and 200) and for two Cauchy numbers, $Ca = 10^{-4}$, and $Ca = 10^{-7}$, while also evaluating the effect of the fin position, as illustrated in Figures 14-16.

Figures 14(a) and 14(b) represent the local Nusselt number for position 1. At the start of the step, the local Nusselt number rises quickly, and this increase becomes more pronounced with higher Reynolds numbers. For Ca=10^{-4} the local Nusselt number increases from about Nu_x=3.55 for Re = 50 at x/H = 10.85 to around Nu_x=8.31 for Re = 200. After reaching the maximum, the curve drops sharply and then stabilizes, maintaining approximately the same value up to the outlet of the channel. The position of the fin seems to have little effect on this overall shape, but the Cauchy number clearly changes the magnitude of the peak. When $Ca = 10^{-7}$ (rigid fin), the maximum value becomes higher, reaching 4.83 for Re = 50 and about 10.44 for Re = 200. This corresponds to an increase of approximately 36% and 25%, respectively. This trend is explained by the limited deformation of a more rigid fin, which maintains a steadier flow pattern and promotes stronger heat exchange close to the heated wall. Downstream, the effect fades, and the curves become similar again.

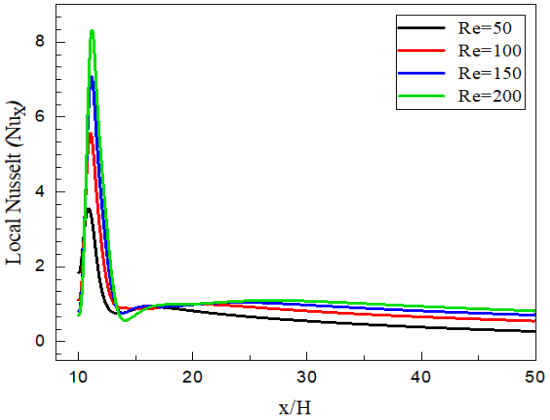

(a) *Ca*=10^{-4}

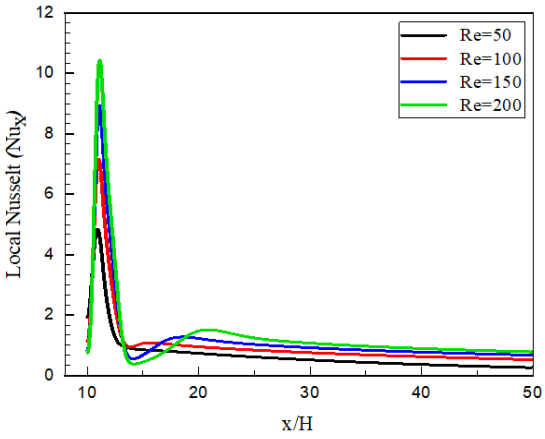

(b) *Ca*=10^{-7}

Fig. 14. The local distribution of the Nusselt number at position 1 for different Reynolds numbers

Figures 15(a) and 15(b) illustrate the local Nusselt number distribution for position 2. For Ca=10^{-4}, the local Nusselt number rises at x/H = 10.97 from approximately Nu_x=3.74 for Re = 50 to about Nu_x=8.26 for Re = 200. After reaching its peak, the curve rapidly declines before leveling off, maintaining nearly the same value toward the outlet. The Cauchy number has a noticeable influence on the peak amplitude. For $Ca = 10^{-7}$, the maximum value is higher, reaching Nu_x=4.9 at Re = 50, Nu_x=7.11 at Re = 100, Nu_x=8.86 at Re = 150 and about Nu_x=10.37 for Re = 200. These results highlight the role of both the Reynolds number and the Cauchy number in influencing the heat transfer field.

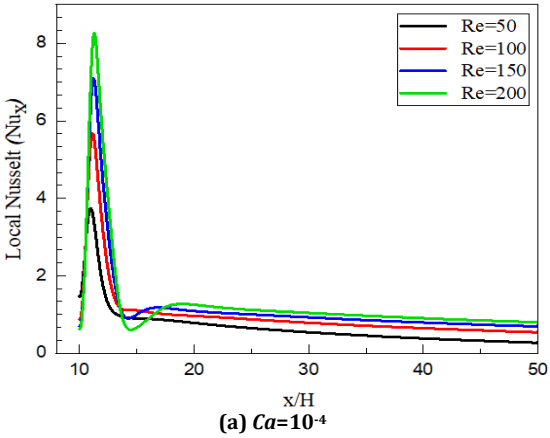

(a) Ca=10^{-4}

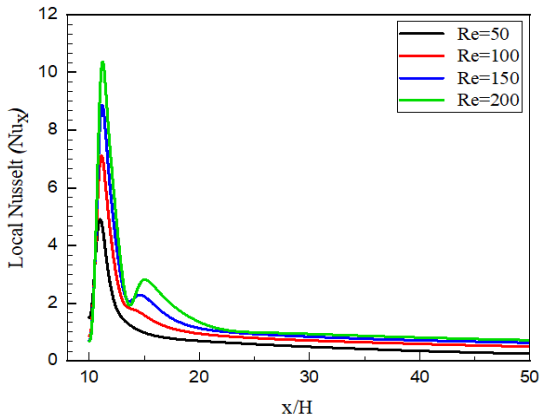

(b) Ca=10^{-7}

Fig. 15. The local distribution of the Nusselt number at position 2 for different Reynolds numbers

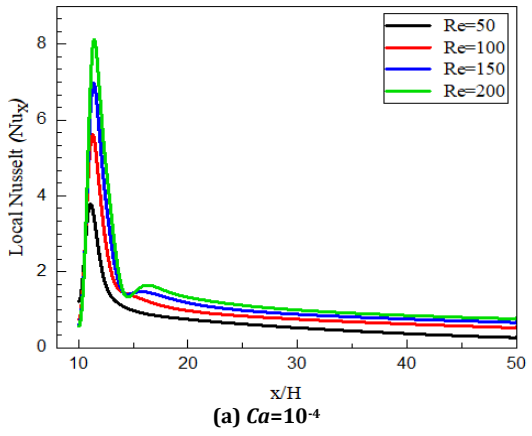

(a) Ca=10^{-4}

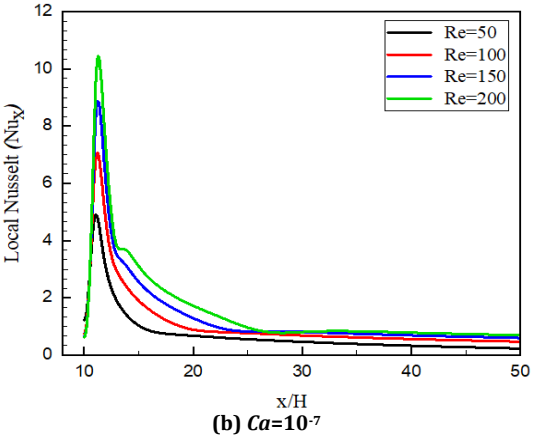

(b) Ca=10^{-7}

Fig. 16. The local distribution of the Nusselt number at position 3 for different Reynolds numbers

Figures 16(a) and 16(b) show the variation of the local Nusselt number for position 3.

At the start of the step, the local Nusselt number shows a steep increase, which becomes more noticeable as the Reynolds number rises. Specifically, at x/H = 11.1 the peak values being Nu_x=3.79 for Re = 50, Nu_x=5.62 for Re = 100, Nu_x=6.98 for Re = 150 and Nu_x=8.12 for Re = 200.

Once the peak is reached, the curve quickly declines before leveling off, keeping an almost constant value toward the outlet.

The Cauchy number has a clear influence on the peak value: for Ca = 10^{-7}, the maximum is higher, reaching Nu_x=4.9 at Re = 50, Nu_x=7.06 at Re = 100, Nu_x=8.87 at Re = 150, and around Nu_x=10.44 at Re = 200, representing an increase of roughly 29.29%, 25.62%, 27.08% and 28.43% respectively.

This trend is explained by the limited deformation of the more rigid fin, which maintains a steadier flow pattern and promotes stronger heat exchange close to the heated wall.

5.6. Maximum Nusselt Number

Figures 17(a) and 17(b) show the evolution of the maximum Nusselt number as a function of the Reynolds number, for different fin positions, and compare it with the case without a fin and the Cauchy number (10^{-4} and 10^{-7}). We observe a gradual evolution depending on the Reynolds number. This progression is almost flat in the case without a fin, and becomes more significant in our cases across the different positions.

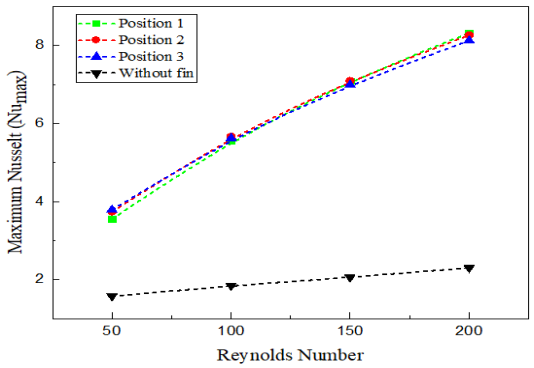

(a) Ca=10^{-4}

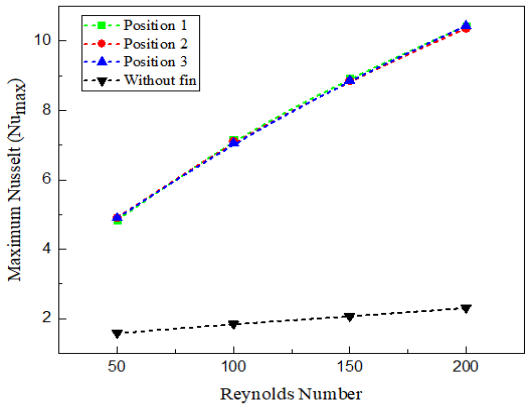

(b) Ca=10^{-7}

Fig. 17. Maximum Nusselt number as a function of Reynolds number at (a) Ca=10^{-4}; (b) Ca=10^{-7}

We note that the position has no impact on this parameter; only the presence of the fin adds to the values of the maximum Nusselt number. For example, for Re= 50 and Ca=10^{-4}, the Nu_{max} values increase from 1.57 (for the case without fin) to 3.78 (for our cases with fin), representing an increase of 140.76 %. However, at Re = 200, this difference becomes more significant: with 2.3 for the case without fins, and 8.31 for our cases with fins, reflecting an increase of 261.3%. For the Ca=10^{-7} case, similar observations can be made with larger variations, starting at 212.1% for the Re = 50 case and rising to 353.91% for the Re = 200. These findings confirm the crucial role of the fin in promoting convective heat transfer downstream of the step.

6. Conclusions

A numerical simulation study of the fluid flow and forced convection in a backward-facing step containing an elastic V-shaped fin has been conducted in the present study. The partial differential equations were solved using a finite element scheme based on the Galerkin method.

The analysis of the forced convection heat transfer phenomenon was carried out by proposing a study for different values of Reynolds number, Cauchy number, and fin position.

Comparisons with the results published in the literature were carried out, and a good agreement was found. The following conclusions can be summarized:

- The average Nusselt number increases as inertial forces dominate viscous forces (Reynolds number increases).
- Regardless of the Reynolds number, Cauchy number, or fin position, the presence of the fin increases the Nusselt number.
- Installing a V-fin in positions two and three with a low Cauchy number (Ca = 10^{-7}) almost doubles the Nusselt number compared to the geometry without the fin.
- In position one, the thermal boundary layer downstream of the fin is highly developed, whatever the Reynolds number and elasticity, resulting in a lower Nusselt number for this position.
- When the fin is highly elastic, the downstream vortex is reduced, the upper part of the fin is deformed, and the flow in this zone (above the fin) is not slowed down.
- The third fin position, close to the top wall, increases the Nusselt number significantly, as most of the flow is directed towards the hot wall.
- For highly elastic fins (large Ca), whatever the fin position, the flow passes through both sides of the fin; when the fin is rigid and in position three, all the flow is directed towards the hot wall.

The results of the present work are of particular interest for industrial applications where heat transfer performance is critical. The proposed configuration to place V-shaped elastic fins offers a twofold advantage: it does not decelerate the flow for highly elastic fins, and it significantly increases heat transfer, especially for rigid fins. Ultimately, the fin position and elasticity control both the hydrodynamic and thermal behavior of the fluid.

Nomenclature

avg	Average value
Ca	Cauchy number, $\rho {U_0}^2/E$
Cp	Thermal specific heat $(J/kg.K)$
D_s	Displacement dynamics
d_s	Fin displacement vector
E	Young's modulus (Pa)
H	Inlet step height
h	Heat transfer coefficient, $(W/m^2.K)$
k	Thermal conductivity $(W/m.K)$
L	Downstream channel length
Nu_x	Local Nusselt number
Nu_{avg}	Average Nusselt number
Nu_{max}	Maximum Nusselt number
p	Pressure (Pa)
P	Dimensionless Pressure, $p/\rho {U_0}^2$
$P1,P2,P3$	Positions of fin relative to the y-axis
Pr	Prandtl number, $\mu Cp/k$

ΔP	Dimensionless pressure drop
Re	Reynolds number, $\mathrm{Re} = \rho U_0 H / \mu$
T	Temperature (K)
T_h	Hot Temperature (K)
T_c	Cold Temperature (K)
u,v	Velocity (m/s)
U,V	Dimensionless velocity, $U = \frac{u}{U_0}$, $V = v/U_0$
U_0	Average inlet velocity (m/s)

Greek characters

τ	Dimensionless time, $\tau = t\ U_0/H$
θ	Dimensionless temperature, $(T - T_c)\ /\ (T_h - T_c)$
α_r	Thermal conductivity ratio
α_s	Thermal diffusivity of solid
α_f	Thermal diffusivity of fluid
ρ_r	Density ratio
μ	Dynamic viscosity ($kg/m.s$)
ρ	Density (kg/m^3)

Funding Statement

This research did not receive any specific grant from funding agencies in the public, commercial, or not-for-profit sectors.

Conflicts of Interest

The author declares that there is no conflict of interest regarding the publication of this article.

Authors Contribution Statement

Ikram Djellid: Conceptualization; Investigation; Validation; Data Curation; Roles/Writing – Original Draft.

Noureddine Bouhamri: Project administration; Supervision; Writing – Review & Editing.

Mohamed Bouhafs: Formal Analysis; Supervision.

Mohamed Bouzit: Methodology; Conceptualization.

Ikram Boualem: Writing – Review & Editing; Validation.

References

[1] Shahabadi, M., Mehryan, S.A.M., Ghalambaz, M. and Ismael, M., 2021. Controlling the natural convection of a non-Newtonian fluid using a flexible fin. *Applied Mathematical Modelling*, 92, pp. 669–86.

[2] Yaseen, D.T. and Ismael, M.A., 2020. Analysis of power law fluid-structure interaction in an open trapezoidal cavity. *International Journal of Mechanical Sciences*, 174, p. 105481.

[3] Mahmood, F.T., Das, A., Smriti, R.B., Hakim, Md. A., Saha, S. and Hasan, M.N., 2023. Role of wall-mounted flexible flow modulator on thermo-hydraulic characteristics of pulsating channel flow. *Results in Engineering*, 17, p. 100941.

[4] Alsabery, A.I., Selimefendigil, F., Hashim, I., Chamkha, A.J. and Ghalambaz, M., 2019. Fluid-structure interaction analysis of entropy generation and mixed convection inside a cavity with flexible right wall and heated rotating cylinder. *International Journal of Heat and Mass Transfer*, 140, pp. 331–45.

[5] Ismael, M.A. and Jasim, H.F., 2018. Role of the fluid-structure interaction in mixed convection in a vented cavity. *International Journal of Mechanical Sciences*, 135, pp. 190–202.

[6] Sabbar, W.A., 2018. Fluid-structure interaction of mixed convection in a cavity-channel assembly of flexible wall. *International Journal of Mechanical Sciences*, 144, pp. 1–15.

[7] Saleh, H., Siri, Z. and Hashim, I., 2019. Role of fluid-structure interaction in mixed convection from a circular cylinder in a square enclosure with double flexible oscillating fins. *International Journal of Mechanical Sciences*, 161–162, p. 105080.

[8] Aly, A.M. and Raizah, Z.A.S., 2019. Coupled fluid-structure interactions of natural convection in a ferrofluid using ISPH method. *Alexandria Engineering Journal*, 58(4), pp. 1499–516.

[9] Ghalambaz, M., Jamesahar, E., Ismael, M.A. and Chamkha, A.J., 2017. Fluid-structure interaction study of natural convection heat transfer over a flexible oscillating fin in a square cavity. *International Journal of Thermal Sciences*, 111, pp. 256–73.

[10] Long, T., Huang, C., Hu, D. and Liu, M., 2021. Coupling edge-based smoothed finite element method with smoothed particle hydrodynamics for fluid structure interaction problems. *Ocean Engineering*, 225, p. 108772.

[11] Meng, Z.F., Zhang, A.M., Yan, J.L., Wang, P.P. and Khayyer, A., 2022. A hydroelastic fluid–structure interaction solver based on the Riemann-SPH method. *Computer Methods in Applied Mechanics and Engineering*, 390, p. 114522.

[12] Chen, Y., Yang, J., Liu, Y. and Sung, H.J., 2020. Heat transfer enhancement in a poiseuille channel flow by using multiple wall-mounted flexible flags. *International Journal of Heat and Mass Transfer*, 163, p. 120447.

[13] Hakim, A., 2022. Fluid structure interaction and heat transfer enhancement with dynamic flexible flow modulator. *International Communications in Heat and Mass Transfer*, 137, p. 106263.

[14] Tabatabaei Malazi, M., Eren, E.T., Luo, J., Mi, S. and Temir, G., 2020. Three-dimensional fluid–structure interaction case study on elastic beam. *Journal of Marine Science and Engineering*, 8(9), p. 714.

[15] Alsabery, A.I., Sheremet, M.A., Ghalambaz, M., Chamkha, A.J. and Hashim, I., 2018. Fluid-structure interaction in natural convection heat transfer in an oblique cavity with a flexible oscillating fin and partial heating. *Applied Thermal Engineering*, 145, pp. 80–97.

[16] Jamesahar, E., Ghalambaz, M. and Chamkha, A.J., 2016. Fluid–solid interaction in natural convection heat transfer in a square cavity with a perfectly thermal-conductive flexible diagonal partition. *International Journal of Heat and Mass Transfer*, 100, pp. 303–19.

[17] Mehryan, S.A.M., Ghalambaz, M., Ismael, M.A. and Chamkha, A.J., 2017. Analysis of fluid-solid interaction in MHD natural convection in a square cavity equally partitioned by a vertical flexible membrane. *Journal of Magnetism and Magnetic Materials*, 424, pp. 161–73.

[18] Raisi, A. and Arvin, I., 2018. A numerical study of the effect of fluid-structure interaction on transient natural convection in an air-filled square cavity. *International Journal of Thermal Sciences*, 128, pp. 1–14.

[19] Mehryan, S.A.M., Alsabery, A., Modir, A., Izadpanahi, E. and Ghalambaz, M., 2020. Fluid-structure interaction of a hot flexible thin plate inside an enclosure. *International Journal of Thermal Sciences*, 153, p. 106340.

[20] Saleh, H., Hashim, I., Jamesahar, E. and Ghalambaz, M., 2020. Effects of flexible fin on natural convection in enclosure partially-filled with porous medium. *Alexandria Engineering Journal*, 59(5), pp. 3515–29.

[21] Saleh, H., Naganthran, K., Hashim, I., Ghalambaz, M. and Nazar, R., 2022. Role of fluid-structure interaction in free convection in square open cavity with double flexible oscillating fins. *Alexandria Engineering Journal*, 61(2), pp. 1217–34.

[22] Ghalambaz, M., Mehryan, S.A.M., Alsabery, A.I., Hajjar, A., Izadi, M. and Chamkha, A., 2020. Controlling the natural convection flow through a flexible baffle in an L-shaped enclosure. *Meccanica*, 55(8), pp. 1561–84.

[23] Khanafer, K. and Vafai, K., 2020. Effect of a circular cylinder and flexible wall on natural convective heat transfer characteristics in a cavity filled with a porous medium. *Applied Thermal Engineering*, 181, p. 115989.

[24] Ghalambaz, M., Mehryan, S.A.M., Feeoj, R.K., Hajjar, A., Hashim, I. and Babaei Mahani, R., 2022. Free convective heat transfer of a non-Newtonian fluid in a cavity containing a thin flexible heater plate: an Eulerian–Lagrangian approach. *Journal of Thermal Analysis and Calorimetry*, 147(2), pp. 1809–24.

[25] Selimefendigil, F. and Öztop, H.F., 2016. Analysis of MHD mixed convection in a flexible walled and nanofluids filled lid-driven cavity with volumetric heat generation. *International Journal of Mechanical Sciences*, 118, pp. 113–24.

[26] Hussain, S. and Ahmed, S.E., 2019. Unsteady MHD forced convection over a backward facing step including a rotating cylinder utilizing Fe_3O_4-water ferrofluid. *Journal of Magnetism and Magnetic Materials*, 484, pp. 356–66.

[27] Toumi, M., Bouzit, M., Bouzit, F. and Mokhefi, A., 2022. MHD Forced Convection Using Ferrofluid Over a Backward Facing Step Containing a Finned Cylinder. *Acta Mechanica et Automatica*, 16(1), pp. 70–81.

[28] Toumi, M., Bouzit, M., Mokhefi, A. and Derbal, D., 2022. Unsteady numerical investigation of ferrofluid forced convection over a downward step containing a rotating finned cylinder. *JSSCM*, 16(2), pp. 67–86.

[29] Abu Talib, A.R. and Hilo, A.K., 2021. Fluid flow and heat transfer over corrugated backward facing step channel. *Case Studies in Thermal Engineering*, 24, p. 100862.

[30] Abu-Nada, E., 2008. Application of nanofluids for heat transfer enhancement of separated flows encountered in a backward facing step. *International Journal of Heat and Fluid Flow*, 29(1), pp. 242–9.

[31] Togun, H., Safaei, M.R., Sadri, R., Kazi, S.N., Badarudin, A., Hooman, K. and Sadeghinezhad, E., 2014. Numerical simulation of laminar to turbulent nanofluid flow and heat transfer over a backward-facing step. *Applied Mathematics and Computation*, 239, pp. 153–70.

[32] Rashid, F.L., Eleiwi, M.A., Tahseen, T.A., Mohammed, H.I., Tuama, S.A., Ameen, A. and Agyekum, E.B., 2025. Influence of adiabatic semi-circular grooved in backward-facing step on thermal-hydraulic characteristics of nanofluid. *International Journal of Thermofluids*, 26, p. 101052.

[33] Abbassi, H. and Ben Nassrallah, S., 2007. MHD flow and heat transfer in a backward-facing step. *International Communications in Heat and Mass Transfer*, 34(2), pp. 231–7.

[34] Hilo, A.K., Abu Talib, A.R., Acosta Iborra, A., Thariq Hameed Sultan, M. and Faisal Abdul Hamid, M., 2020. Effect of corrugated wall combined with backward-facing step channel on fluid flow and heat transfer. *Energy*, 190, p. 116294.

[35] Xie, W.A. and Xi, G.N., 2017. Fluid flow and heat transfer characteristics of separation and reattachment flow over a backward-facing step. *International Journal of Refrigeration*, 74, pp. 177–89.

[36] Alhasan, M., Hamzah, H., Koprulu, A. and Sahin, B., 2024. Couette-Poiseuille flow over a backward-facing step: Investigating hydrothermal performance and irreversibility analysis. *Case Studies in Thermal Engineering*, 53, p. 103954.

[37] Atashafrooz, M., 2020. Influence of radiative heat transfer on the thermal characteristics of nanofluid flow over an inclined step in the presence of an axial magnetic field. *Journal of Thermal Analysis and Calorimetry*, 139(5), pp. 3345–60.

[38] Danane, F., Boudiaf, A., Mahfoud, O., Ouyahia, S.-E., Labsi, N. and Khaled Benkahla, Y., 2020. Effect of backward facing step shape on 3D mixed convection of Bingham fluid. *International Journal of Thermal Sciences*, 147, p. 106116.

[39] Zamzari, F., Mehrez, Z., El Cafsi, A., Belghith, A. and Le Quéré, P., 2017. Numerical investigation of entropy generation and heat transfer of pulsating flow in a horizontal channel with an open cavity. *Journal of Hydrodynamics*, 29(4), pp. 632–46.

[40] Zamzari, F., Mehrez, Z. and El Cafsi, A., 2019. Heat Transfer Enhancement of Pulsating Flow in an Open Cavity Subjected to Uniform Magnetic Field. *Fluid Dynamics*, 54(3), pp. 428–38.

[41] Abdulkarim, A.H., Eleiwi, M.A., Tahseen, T.A. and Canli, E., 2021. Numerical Forced Convection Heat Transfer of Nanofluids over Back Facing Step and Through Heated Circular Grooves. *Mathematical Modelling of Engineering Problems*, 8(4), pp. 597–610.

[42] Bahrami, H.-R., 2021. Numerical investigation of flow and heat transfer behind a two-dimensional backward-facing step equipped with a semi-porous baffle. *Journal of Central South University*, 28, pp. 3354–3367.

[43] Rashid, F.L., Eleiwi, M.A., Tahseen, T.A., Mohammed, H.I., Tuama, S.A., Ameen, A. and Agyekum, E.B., 2025. Influence of adiabatic semi-circular grooved in backward-facing step on thermal-hydraulic characteristics of nanofluid. *International Journal of Thermofluids*, 26, p. 101052.

[44] Siavashi, M., Talesh Bahrami, H.R. and Aminian, E., 2018. Optimization of heat transfer enhancement and pumping power of a heat exchanger tube using nanofluid with gradient and multi-layered porous foams. *Applied Thermal Engineering*, 138, pp. 465–474.

[45] Siavashi, M., Talesh Bahrami, H.R. and Saffari, H., 2015. Numerical investigation of flow characteristics, heat transfer and entropy generation of nanofluid flow inside an annular pipe partially or completely filled with porous media using two-phase mixture model. *Energy*, 93, pp. 2451–2466.

[46] Talaei, H. and Bahrami, H.-R., 2023. Backward-facing step heat transfer enhancement: a systematic study using porous baffles with different shapes and locations and corrugating after step wall. *Heat and Mass Transfer*, 59, pp. 2213–2230.

[47] Kumar, A. and Dhiman, A.K., 2012. Effect of a circular cylinder on separated forced convection at a backward-facing step. *International Journal of Thermal Sciences*, 52, pp. 176–85.